RSC Advances

PAPER

Cite this: *RSC Adv.*, 2020, **10**, 13879

Synthesis and antibacterial activity of iron manganite ($FeMnO_3$) particles against the environmental bacterium *Bacillus subtilis*†

Zorka Z. Vasiljevic,[a] Milena P. Dojcinovic,[b] Jugoslav B. Krstic,[c] Vesna Ribic,[b] Nenad B. Tadic,[d] Milos Ognjanovic,[e] Sandrine Auger,[f] Jasmina Vidic[f] and Maria Vesna Nikolic *[b]

Received 25th February 2020
Accepted 27th March 2020

DOI: 10.1039/d0ra01809k

rsc.li/rsc-advances

Nanocrystalline iron manganite powder was synthesized using the sol–gel combustion process, with glycine as fuel. It was further calcined at 900 °C for 8 h, resulting in the formation of a loose cubic $FeMnO_3$ powder with a small specific surface area, net-like structure and plate-like particles as confirmed by XRD, N_2 physisorption, FESEM and TEM analyses. The metal ion release was studied by ICP-OES and showed that less than 10 ppb of Fe or Mn ions were released by leaching in water, but 0.36 ppm Fe and 3.69 ppm Mn was found in LB (Luria–Bertani) bacterial medium. The generation of reactive oxygen species (ROS) was monitored in distilled water and bacterial medium and showed that $FeMnO_3$ particles do not generate $O_2^{\bullet-}$ ions with or without UV irradiation, but synthesize H_2O_2 and show an antioxidative effect. Besides the higher stability of $FeMnO_3$ particles in aqueous solution they showed an inhibitory effect on *Bacillus subtilis* growth in LB medium even at low concentrations (0.01 mg ml^{-1}), but not in BHI medium even at 1 mg ml^{-1}. This study points out that the mechanism of antibacterial action of engineered metal oxides needs continued investigation and specific experimental controls.

Introduction

Metal oxide nanostructures such as nanoparticles, nanowires, nanotubes and nanoporous structures can exhibit diverse physical and chemical properties[1] and their application fields include catalysis, photonics, energy storage and conversion, fuel cells, gas sensing, microelectronics, environmental decontamination, biomedicine and biosensors.[1,2] With the growing application of metal oxide nanostructures increasing amounts are being released into the environment. The toxicity of nanomaterials to bacteria has caused concern, as bacteria have critical roles in the ecosystem.[3–6] Metal oxide particle toxicity can originate from dissolved metals from the oxides.[3] For bacteria, the most recognized mechanism of metal oxide nanoparticle toxicity so far is spontaneous generation of radical oxygen species (ROS) and enhanced oxidative stress.[2,7] Highly reactive ROS can be produced on the surface of metal oxide particles with or without UV illumination.[5,8,9] ROS-induced damages and bacterial death comprise cell metabolite perturbation, oxidative lesions and membrane impairment by lipid peroxidation resulting in cell leakage. In addition, ROS can damage bacterial components such as surface proteins and nucleic acids.[2]

Metal and metal oxide nanoparticles can also show superior activity towards resistant microorganisms.[10–13] Recent research has focused on metal oxides consisting of two or more metallic compounds where beneficial synergistic effects of their components are combined, especially as potential antimicrobial agents.[2,5] Iron-containing nanoparticles are widely applied and generally found to be non-toxic expressing no antimicrobial activity, but co-exposure of nanoparticles and known pathogens can impact host innate immunity.[6] Antimicrobial activity of manganese and iron doped zinc oxide nanoparticles was investigated by Sharma *et al.*[14] showing that the synergistic effect of co-doping with Mn and Fe resulted in an enhanced antimicrobial effect and photocatalytic degradation. Spinel ferrites are widely utilized as magnetic materials in microelectronics and medicine, but also can have antimicrobial properties.[12] Manganese oxides and their composites are also applied as adsorbents for the removal of metal ions and contaminants from waste water.[15]

[a]*Institute of Technical Sciences of SASA, Belgrade, Serbia*
[b]*Institute for Multidisciplinary Research, University of Belgrade, Belgrade, Serbia. E-mail: mariav@rcub.bg.ac.rs*
[c]*Department of Catalysis and Chemical Engineering, Institute of Chemistry, Technology and Metallurgy, University of Belgrade, Belgrade, Serbia*
[d]*Faculty of Physics, University of Belgrade, Belgrade, Serbia*
[e]*Institute of Nuclear Sciences Vinca, University of Belgrade, Belgrade, Serbia*
[f]*Micalis Institute, INRA, AgroParisTech, Université Paris-Saclay, 78350, Jouy-en-Josas, France. E-mail: jasmina.vidic@inrae.fr*

† Electronic supplementary information (ESI) available. See DOI: 10.1039/d0ra01809k

Mixed iron manganese oxides due to their earth abundance, low toxicity, magnetic properties, high electrical conductivity and ease of preparation have been the subject of much research.[16] Among them, iron manganite ($FeMnO_3$) has recently been investigated for application as a lithium-ion battery anode material,[16,17] catalyst,[18] energy storage,[19–21] humidity sensor[22,23] and for photocatalysis.[24,25]

Research has also focused on the synthesis process of iron manganite. Besides mechano-synthesis by ball milling[26] or solid state synthesis,[23] nanostructured iron manganite powder has been obtained by co-precipitation,[24,27] hydrothermal synthesis[16,17,22] and sol–gel combustion using different agents, such as glycine,[28] urea,[27] ethylenediamine[29] and polyvinyl alcohol.[18]

In this work we performed synthesis of iron manganite ($FeMnO_3$) by sol–gel combustion using glycine as fuel and a detailed structural, morphological and textural characterization of the obtained particles. For the first time, $FeMnO_3$, was investigated in solutions and tested for its antibacterial impact. *Bacillus subtilis* was used as a model soil bacterium as it is a well-characterized microorganism widely utilized in biotechnology.[30,31]

Results and discussion

XRD analysis

Iron manganite produced by the combustion synthesis route using glycine as fuel is shown in Fig. S1.† The measured XRD pattern of the obtained $FeMnO_3$ powder showed sharp and intense peaks belonging to the cubic space group $Ia\bar{3}$ (bixbyite) for pure iron manganite powder (Fig. 1a). The Rietveld refinement curve (wR 3.26%) is shown as an inset in Fig. 1a. The determined unit cell parameter was $a = 9.4195(4)$, crystallite size 93 nm and microstrain $1.4(4) \times 10^{-3}$. The atomic positions and interatomic distances are given in Table S1.† The crystal structure with these parameters has been drawn using the VESTA software[32] (Fig. 1b). In the bixbyite cubic structure Fe and Mn ions are randomly distributed in a 1 : 1 ratio on 8a and 24d crystallographic sites.[29,33] Fe ions are green and Mn ions are purple halves of the balls shown in Fig. 1b. They represent metal ions at the centre of a cube of oxygen denoted as red balls in Fig. 1b. Two oxygen sites are vacant.

The two vacancies are distributed over 8 sites by forming the ends of a face diagonal of a cube of oxygen or by forming the ends of a body diagonal and their centres are a and b sites, respectively[34] Iron and manganese ions are in a regular octahedral environment on 8a sites, while it is distorted on 24d sites.[33]

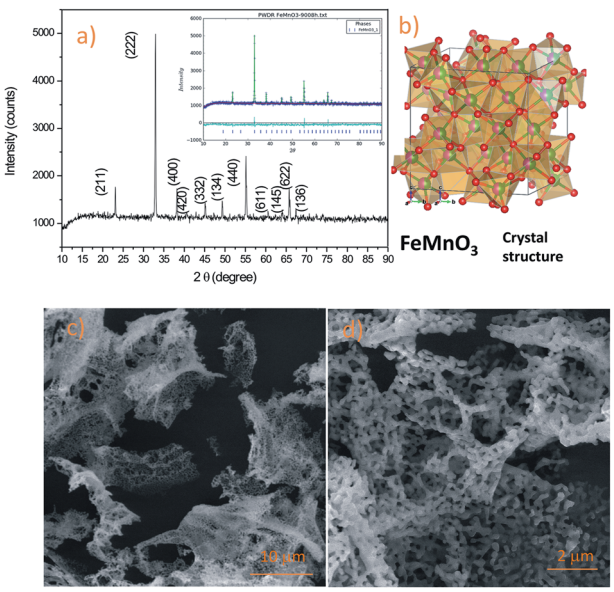

Fig. 1 XRD pattern, inset Rietveld analysis (a), crystal structure drawn using VESTA[31] (b) and FESEM images (c), (d) of $FeMnO_3$ powder.

FESEM and TEM images

FESEM images of the FeMnO3 powder (Fig. 1c and d) show the obtained net-like loose structure. This is further confirmed by

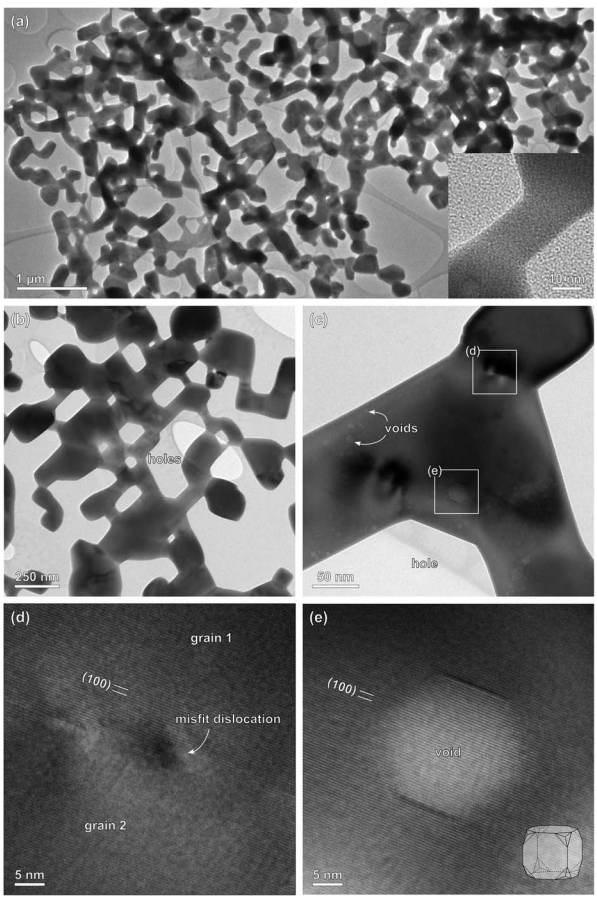

Fig. 2 TEM image of $FeMnO_3$ powder microstructure, the inset shows a neck between two sections of the same grain with large holes formed due to rapid crystallization, (a) TEM image of one grain intercepted with large holes, (b) TEM image of crystal sheets with voids (marked with arrows), hole and domain, (c) HRTEM images representing crystal structure of the segments from image (c), a semi-coherent interface between two grains with a misfit dislocation (d), and an euhedral void with clinographic projection of bixbyite crystal shape is presented in the bottom right corner of the image (e).

TEM images shown in Fig. 2. Fig. 2a shows a net-like structure composed of plate-like particles characterized by a substantially exposed outer surface. Individual particles are relatively large, ranging from 0.2–1 μm but very macroporous and thin. Their morphology originates from the rapid combustion process that generates thin crystal sheets with macropores enclosing gas pockets, which are the consequence of the Kirkendall effect and trapped gasses produced in the course of the combustion process.

Internal surfaces of porous crystalline sheets adopt low energy planes of the bixbyite structure. Fig. 2b shows one such crystal sheet intercepted with large holes and smaller voids. Fig. 2c displays the internal structure of net-like crystal sheets, composed of smaller interconnected sub-grains with enclosed voids with diameters of 3–20 nm. The average sub-grain size was 180 ± 64 nm, measured over 22 particles. This is somewhat larger than the particle diameter (crystallite size) estimated by Rietveld analysis of XRD data, which underestimates the particle size when these exceed 100 nm. Assuming cubic morphology of sub-grains, the calculated specific surface area (SSA) for the average particle size measured from TEM images is 6.7 $m^2 g^{-1}$. Estimated from TEM images about 10–20% of the particles' surface area is interconnected. The lattice image in Fig. 2d indicates an interface between two grains in close crystallographic orientation. Just a misfit dislocation on the interface indicates that their orientation was most likely adopted through coalescence that brought the two crystals in almost identical orientation, forming some kind of network structure of interconnected grains along (001) facets. Fig. 2e shows a euhedral void enclosed within the $FeMnO_3$ crystal. (002) lattice planes are parallel to one set of forms that confine the pore. The *d*-values of (001) planes from lattice images correspond to *d*(001) from our XRD measurements. Similar to holes, the voids also have a distinct morphology, faceted by low-index lattice planes.

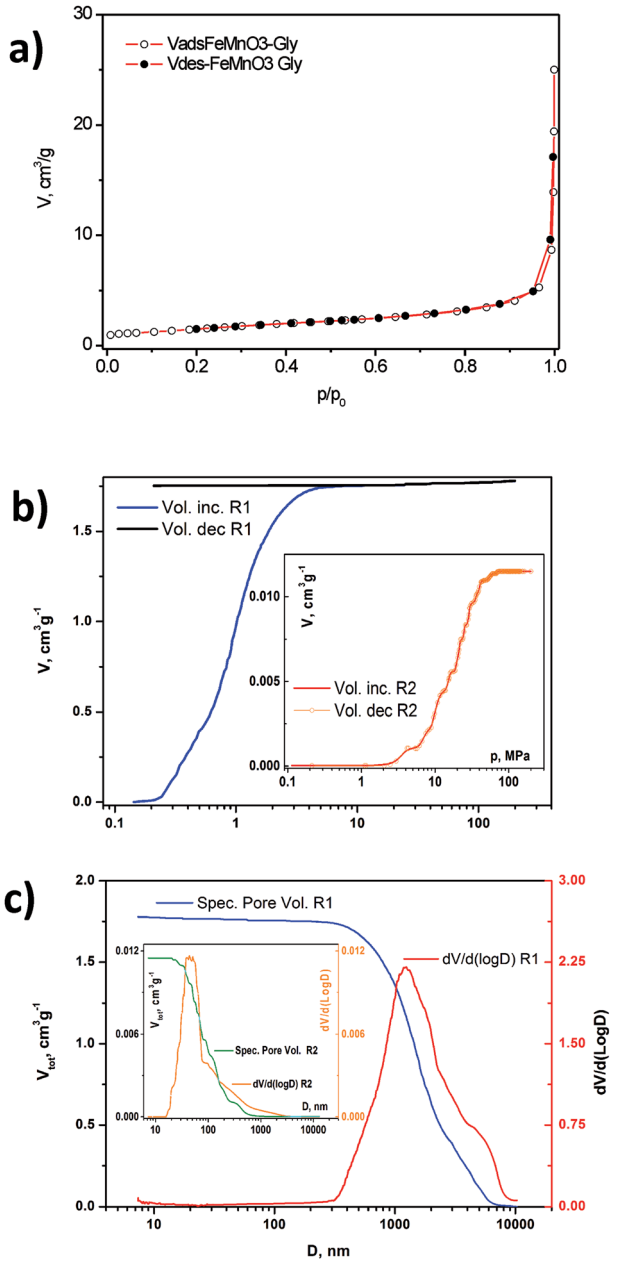

Fig. 3 N_2 isotherm (a), Hg porosimetry measurements (b) and (c) of $FeMnO_3$ powder.

Textural characterization

The shape of the nitrogen isotherm (Fig. 3a), almost complete overlap of adsorption and desorption branches, small values of adsorbed N_2 volume (0.010 $cm^3 g^{-1}$ at $p/p_0 = 0.98$) and BET specific surface area of 5.6 $m^2 g^{-1}$ classify the isotherm in type II according to IUPAC nomenclature.[35] The type II isotherms are characteristic for non-porous or macroporous materials. The volume of micropores calculated from the α-S plot was also small 0.003 $cm^3 g^{-1}$. These results are in accordance with Cao *et al.*[17] who prepared $FeMnO_3$ by a hydrothermal method. Hg porosimetry in two consecutive intrusion–extrusion runs was conducted in order to further resolve the textural characteristics of $FeMnO_3$ (shown in Fig. 3b and c). The low value of bulk density (0.464 g cm^{-3}) obtained from run 1 confirmed the loose nature of the synthesized $FeMnO_3$ powder. The total intruded Hg volume during the first run is markedly high giving overall values of the total cumulative volume of 1.760 $cm^3 g^{-1}$ and porosity higher than 82%. In this high porosity value, at least some part must originate from macropores recognized on TEM micrographs (Fig. 2) and the net-like structure containing plate-like particles. However, the calculated specific surface area obtained for the cylindrical pore model was 11.2 $m^2 g^{-1}$. This value is higher than the BET values obtained by N_2 physisorption measurement and the SSA value calculated from TEM images. These unusual results suggest that at least some of the intruded Hg volume does not come from intrusion into the pore system but from entry into interparticle voids. Although, the shape of extrusion branch of the first run (almost completely parallel to the *x*-axis) can be interpreted as a consequence of ink-bottle shaped pores present in $FeMnO_3$ powder, the absence of a hysteresis loop in the N_2 isotherm, and no evidence of their existence in TEM micrographs, confirm that interparticle space

presents a significant component of the measured porosity. Moreover, the second run shows that only a small amount of Hg can fill the pore system, and the extrusion brunch is completely reversible to the intrusion one. It is interesting to notice that, the measured total pore volume of N_2 and the total pore volume determined by run 2 are very close each other (0.010 $cm^3\ g^{-1}$ *vs.* 0.011 $cm^3\ g^{-1}$). One assumption is that a significant part of the porous structure is not available during the second cycle measurement as the 2D particles forming a net-like structure have compacted and packed during pressurization in the first measuring run.

UV-vis DRS analysis

The Tauc model for a direct system was used to calculate the optical band gap of $FeMnO_3$ from the measured diffuse reflection spectrum (Fig. 4a), assuming direct transition from valence to conductance band.[36] The equivalent absorption coefficient was calculated from measured diffuse reflectance spectra using the Kubelka–Munk transformation.[37] It was determined to be 1.69 eV that is slightly lower than the values determined by Habibi and Mosavi of 1.901 (ref. 24) and 2.014 eV (ref. 25) depending on the synthesis procedure and molar ratio of the starting precursors. Bin *et al.*[38] performed first principle calculations predicting a very small gap in one spin channel and a relatively large gap in the opposite spin channel.

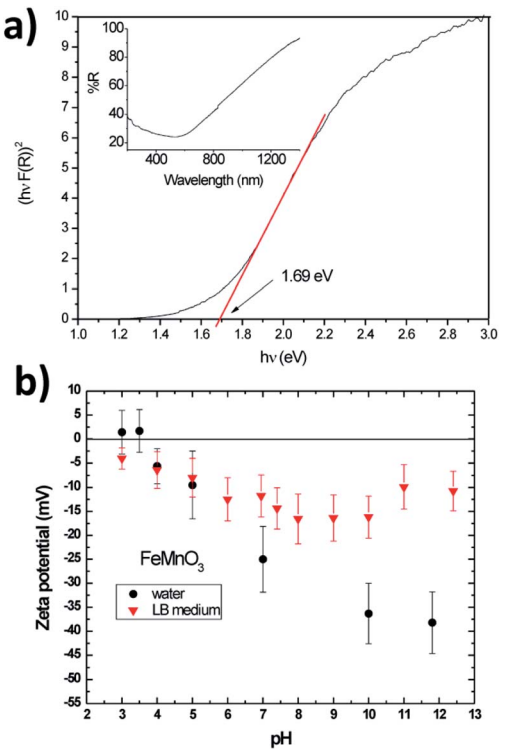

Fig. 4 UV/Vis DRS spectra (inset) and Tauc plot for allowed direct transition of $FeMnO_3$ powder (a) and zeta potential as a function of pH determined for $FeMnO_3$ particles (b).

Colloidal properties

To get insight into the colloidal properties of $FeMnO_3$ particles in solution, they were characterized by DLS and zeta-sizer for their sizes and surface charges, respectively. The hydrodynamic particle diameter in water was determined as 242 ± 27 nm confirming the particle size determined from TEM images indicating that particle aggregation did not take place. In LB medium the particle diameter was determined as 738 ± 25 nm showing that some particle aggregation took place in LB, or molecules from bacterial medium adsorbed on iron manganite.

The zeta potential of $FeMnO_3$ particles in water suspension at room temperature was −25.8 ± 4.8 mV. The negative charge value was relatively high, indicating particle stability in water solution. In LB medium the zeta potential at room temperature was −11.8 ± 4.4 mV, lower than for water but still negative. The point of zero charge (P_{zc}) at which the zeta potential shifted to zero was determined by varying the pH of the solution and in water was about 3.6 (Fig. 4b). At acidic pHs, lower values of the zeta potential suggest inter-particle attractions and their aggregation. In contrast, at neutral and basic pHs the high absolute values of the zeta potential suggest an electrostatic repulsion between particles, and their stability. In LB medium all zeta potential values were negative (Fig. 4b), with a minimum between pH 8 and 10 and for basic pHs the zeta potential values were lower than in water.

ROS release

As mentioned above, the main antibacterial mechanism reported for metal oxide nanoparticles is ROS-induced oxidative stress.[2] Different types of metal oxide particles produce different types of ROS (such as singlet oxygen ($O_2^{\bullet -}$), superoxide radicals ($O_2^{\bullet -}$), hydroxyl radicals ($^{\bullet}OH$), hydrogen peroxide (H_2O_2)) by reducing dissolved O_2 in water. For instance, MgO and CaO particles can generate singlet oxygen, ZnO can generate H_2O_2 and OH^-, while CuO and ZnMgO particles can produce all types of ROS.[5,7,8] We performed the XTT test to verify whether $FeMnO_3$ particles generate ROS in aqueous solutions. The reduction of XTT by $O_2^{\bullet -}$ ions results in formation of the orange-coloured XTT-formazan which adsorbs at 470 nm.[12] Fig. 5 shows that $FeMnO_3$ particles did not generate $O_2^{\bullet -}$ ions with or without UV irradiation in water nor in biological LB medium as no peak was observed at 470 nm. Surprisingly, $O_2^{\bullet -}$ was detected in LB broth alone exposed to UV (Fig. 5b). The small adsorption peak observed at 470 nm in the XTT test is characteristic for orange-colored XTT-formazan that is formed upon reduction of XTT by $O_2^{\bullet -}$.[12] Further tests would be required to confirm the reason behind this observation. Interestingly, the peak of XTT-formazan decreased when $FeMnO_3$ particles were admixed to LB. A similar effect was observed in BHI medium (Fig. S2†). This result strongly suggests an antioxidant activity of $FeMnO_3$. In addition, $FeMnO_3$ exposed to UV showed higher intensities in UV-vis spectra without showing a peak at 470 nm.

We next performed an XTT assay to evaluate whether $FeMnO_3$ may generate singlet oxygen intracellularly. Besides being reduced by $O_2^{\bullet -}$, XTT can also be cleaved by dehydrogenase enzymes of metabolically active bacterial cells.[39] Thus, the

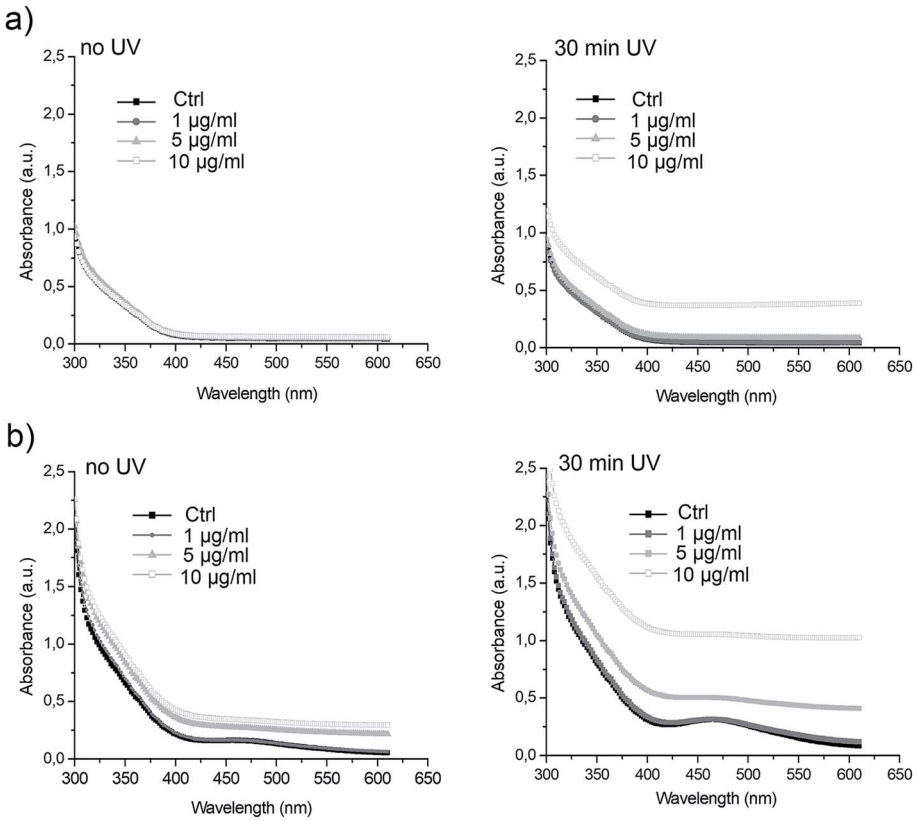

Fig. 5 XTT assay. $FeMnO_3$ at various concentrations was dissolved in water (a) or LB medium (b). Solution was kept in dark (no UV) or exposed to UV irradiation upon 30 min. XTT test was performed then in order to verify ROS formation.

formation of XTT-formazan in a solution containing bacterial cells and $FeMnO_3$ would reflect two phenomena: bacterial viability/proliferation and generation of $O_2^{\bullet -}$ ions. Fig. 6a shows that 10^6 CFU ml^{-1} of *B. subtilis* cells efficiently reduced XTT leading to an adsorption maximum at wavelengths between 440–490 nm. Cell proliferation in LB medium over time led to the peak intensity increase. When the same measurement was performed in the presence of 1 mg ml^{-1} $FeMnO_3$ a significant peak intensity decrease was observed at all times measured (Fig. 6b). This suggests an antibacterial activity of $FeMnO_3$ as it inhibited bacterial viability/proliferation.

To verify whether $FeMnO_3$ particles may generate intracellularly other ROS, such as hydrogen peroxide (H_2O_2) or hydroxyl radicals ($^{\bullet}OH$), the DCFH-DA assay was performed. Bacterial cells are permeable for this probe, which can be hydrolyzed intracellularly by a two-electron oxidation to the fluorescent DCF carboxylate anion. The basal production of ROS by bacterial cells due to aerobic metabolism was determined using 10^6 CFU ml^{-1} *B. subtilis* cells in LB medium in the presence of 200 µM DCFH-DA. Fig. 6c shows kinetics of DCFH-DA oxidation in such non-stress conditions (black line). However, presence of 1 mg ml^{-1} $FeMnO_3$ resulted in a significant increase of fluorescence which indicates the high amount of ROS production (red line). This strongly suggests that $FeMnO_3$ generates ROS like $^{\bullet}OH$ and H_2O_2, that is potentially toxic for bacterial cells.

Antioxidant recovery activity

To complete tests, the free radical scavenging activity of DPPH was tested to further evaluate the antioxidant potential of $FeMnO_3$ NPs. The observed DPPH radical scavenging activity of $FeMnO_3$ NPs was dose dependent (Fig. 7a), with the IC_{50} value of 0.06 mg ml^{-1} (Fig. 7b). Such strong DPPH radical scavenging potential of $FeMnO_3$ particles may be due to the particle ability to donate electrons or hydrogen ions as previously shown for silver NPs,[40,41] and/or due to the release of Mn-ions into the solution. Mn-ions have an inherent ability to quench free radical-mediated reactions.[42]

The pH of water and LB medium was measured after adding 1 mg ml^{-1} $FeMnO_3$ to check whether the hydrogen ions availability increased in the presence of $FeMnO_3$. Water and LB medium were of neutral pH before particle admixing (pH ~7). In contrast, the pH value of both solutions containing $FeMnO_3$ was ~6.5, indicating the formation H^+ ions. It is interesting to note that the neutral pH of BHI solution was unchanged after addition of 1 mg ml^{-1} $FeMnO_3$.

ICP-OES analysis was performed to verify whether the $FeMnO_3$ particles released manganese ions in an aqueous solution. In water, the release of both Mn and Fe metal ions after 24 h leaching was about 10 ppb. Surprisingly, the release of Fe and Mn was 0.36 ppm and 3.69 ppm, respectively in LB medium after 24 h. This indicates that the dissolution rate of $FeMnO_3$ in a rich bacterial medium is high.

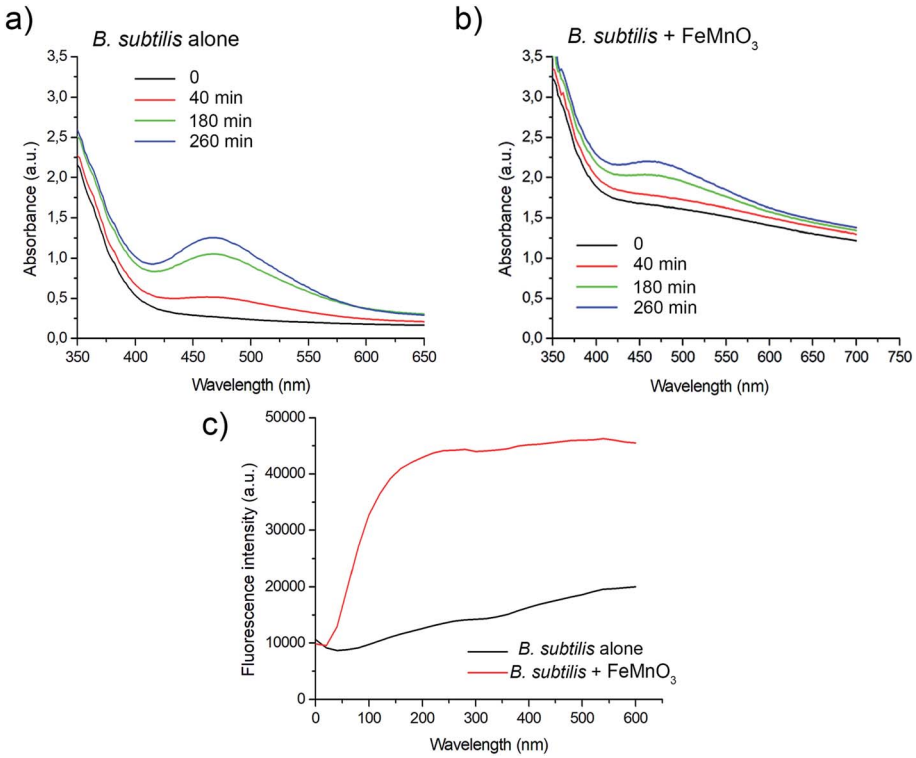

Fig. 6 Intracellular ROS production. (a) Cleavage of XTT by bacterial enzyme dehydrogenase shows cell proliferation with time. (b) XTT assay performed on bacterial cells in the presence of 1 mg ml^{-1} $FeMnO_3$. (c) Change of fluorescence intensity with DCFH-DA oxidation in the presence of $FeMnO_3$ for *B. subtilis*. Each curve is an average of 6 independent measurements.

Low concentrations of Mn-ions (of about 0.18 μM) may have a protecting antioxidant effect on living cells. For instance, bacteria utilize Mn as a key micronutrient to counteract the effects of oxidative stress reactions.[42–44] Mn protects cells from oxidative stress, either as a cofactor for Mn-dependent catalases and superoxide-dismutases or *via* direct quenching. However, high concentrations of Mn ions (of about 66.42 μM) observed in LB medium will hardly be tolerated by bacterial cells, because intracellular metal homeostasis in bacteria is ensured by finely tuned import and efflux systems.[45] It seems that both hydrogen ion generation and Mn-ion release of $FeMnO_3$ particles induce strong DPPH radical scavenging indicating an antioxidant effect.

Bacterial growth inhibition

Previous studies have shown that bacterial cells may neutralize H_2O_2 by catalyse or some superoxide enzymes, and in such way cope with acute oxidative stress.[7,45] We next sought to evaluate for any potential cytotoxicity of $FeMnO_3$ dissolved in bacterial media. The impact of different concentrations of $FeMnO_3$ was

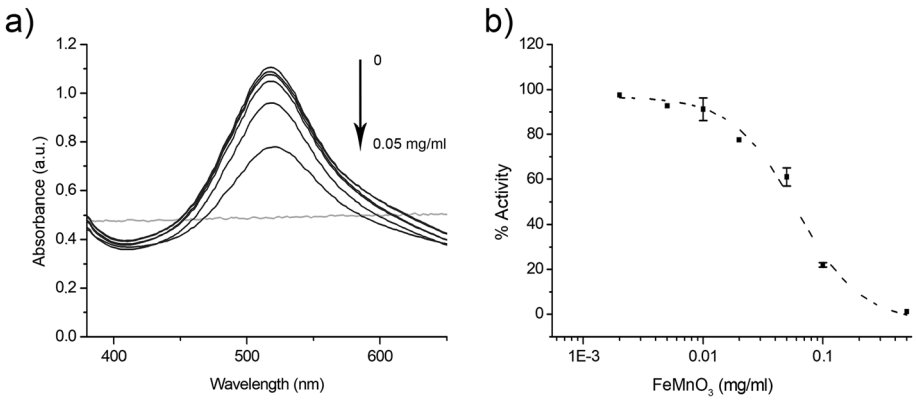

Fig. 7 DPPH assay showing antioxidant activity. IC_{50} 0.06 mg ml^{-1} (a) adsorption curves obtained with increasing concentrations of $FeMnO_3$ particles, grey curve corresponds to particles alone. (b) IC_{50} plot.

studied by measuring grown kinetics of a *B. subtilis* hospital isolate (NDMed). No UV irradiation was performed. Instead, particles were exposed to ambient laboratory light. $FeMnO_3$ significantly affected bacterial growth, even at 0.001 mg ml^{-1} concentration in LB medium (Fig. 8a). However, no antibacterial effect was observed in BHI medium, which is rich in proteins and oligosaccharides (Fig. 8b). These results indicate that the antibacterial effect of $FeMnO_3$ particles depends strongly on the chemical composition of the medium. It is possible that $FeMnO_3$ nanocrystals adsorbed organic molecules from the BHI that passivized their surface by a phenomenon known as protein corona. Corona modifies the surface and activity of particles in biological fluids and media.[2,46] However, this hypothesis still has to be verified experimentally for $FeMnO_3$ in BHI. In contrast, we observed that $FeMnO_3$ released a toxic quantity of Mn-ions in LB medium that contains a significantly lower amount of proteins than BHI.[46] Another possibility is that the pH decrease observed in LB but not in BHI medium after addition of $FeMnO_3$, directly caused the observed bacterial growth inhibition. Overall, our results show that metal ion dissolution and H_2O_2 generation may cause $FeMnO_3$ mediated killing of *B. subtilis* cells. $FeMnO_3$ particles are highly stable in water, but may release high amounts of metal-ions in biological media. *B. subtilis* possesses complex regulatory mechanisms to maintain intracellular Fe- and Mn-ions homeostasis for environmental concentrations, but cannot tolerate concentrations similar to those quantified here for $FeMnO_3$ in LB solution by the ICP-OES analysis.[45,47,48]

Other mechanisms of antibacterial activity of metal oxide particles have been proposed recently. 'Omics' data have indicated that ZnO nanoparticles trigger enzyme inhibition and perturbation in carbohydrate metabolism and bioenergetics in *Staphylococcus aureus* by a ROS independent mechanism.[49] Mixed Mg–ZnO nanoparticles had multimode action on *B. subtilis* cells.[8] Besides the expected bacterial reaction to oxidative stress, *B. subtilis* had modified expression profiles of proteins associated with information processing, metabolism, cell envelope and cell division.[8]

To the best of our knowledge, there is no prior report about the prevalent ROS generated, nor metal ion released in aqueous solutions of $FeMnO_3$ particles. We conducted the study without any bias and found out that, (i) various ROS can be generated, and (ii) both metal ion release and ROS production strongly depended on the surrounding medium. Consequently, it appears that toxicity of $FeMnO_3$ towards environmental bacteria can be regulated by controlling external conditions.

Experimental

Iron(III) nitrate nonahydrate ($Fe(NO_3)_3 \cdot 9H_2O$), manganese(II) nitrate hydrate ($Mn(NO_3)_2 \cdot 6H_2O$) and glycine ($C_2H_5NO_2$) were procured from Sigma Aldrich. All chemicals were of reagent grade and used as received without further purification. Deionized water and ethanol (puriss) used were also from Sigma Aldrich.

Synthesis of iron manganite powder

Ferric nitrate, manganese nitrate and glycine were dissolved separately in deionized water and then magnetically mixed in the nitrate : glycine ratio 1 : 3 at 80 °C until a gel was formed. The temperature was increased to 300 °C and combustion of the gel took place after a few minutes. After slight crushing in an agate mortar the combusted powder was calcined at 900 °C for 8 h, again followed by crushing in an agate mortar.

Iron manganite powder characterization

X-ray diffraction (XRD) patterns were recorded on a Rigaku Ultima IV diffractometer (Japan). The structural parameters were refined using the Rietveld method and the GSAS II software package.[50] Structural refinement was performed assuming the cubic space group $Ia\bar{3}$ for iron manganite, where Fe and Mn ions are randomly distributed in the 1 : 1 ratio on 8a and 24d crystallographic sites. Structural parameters determined previously by Rietveld refinement of X-ray diffraction patterns measured of $FeMnO_3$ powder obtained by solid state synthesis were used as starting parameters.[23] They were obtained using the starting parameters from ICSD 30237.[51]

Field-emission scanning electron microscopy (FESEM) images were recorded on a TESCAN MIRA3 XM FESEM device (Czech Republic). Transmission electron microscopy (TEM) analysis was performed using a conventional 200 kV

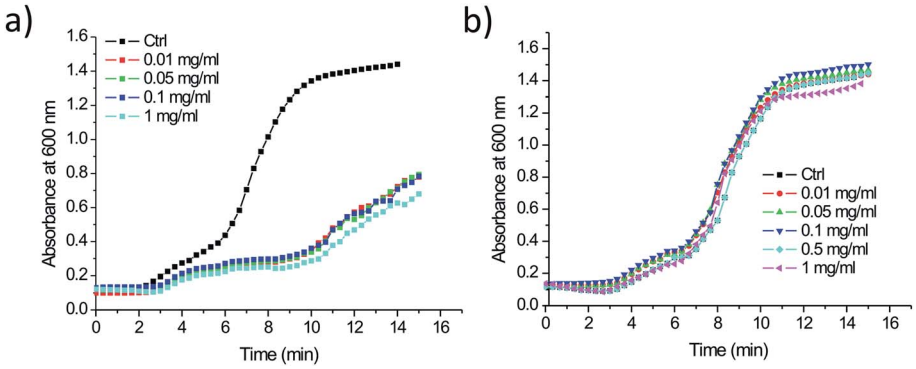

Fig. 8 Growth kinetics of NDmed *B. subtilis* alone or in the presence of different concentrations of $FeMnO_3$ particles in LB (a) and BHI (b).

transmission electron microscope (TEM; JEM-2100, Jeol Ltd., Tokyo, Japan). The sample was prepared by dispersing the $FeMnO_3$ calcined powder in ethanol followed by ultrasonication for 10 min to de-agglomerate the particles. The suspension was applied to a Ni TEM mesh with a perforated carbon film.

UV-vis diffuse reflectance spectra (DRS) were measured on a Shimadzu UV-2600 device with an ISR2600 Plus Integrating sphere attachment (Japan) in the measuring range 200–1400 nm.

The zeta potential of a 0.1 mg ml^{-1} suspension of $FeMnO_3$ powder in deionized water and LB medium was measured at 25 ± 0.1 °C in a disposable zeta cell (DTS 1070) of a NanoZS90 (Malvern, UK) device. Samples were measured after 1 hour of equilibrium time at constant ionic strength of 0.01 M set by NaCl. The particle size by dynamic light scattering (DLS) was determined on a NanoZS90 apparatus (Malvern, UK) with a 4 mW He–Ne laser source ($\lambda = 633$ nm). The stock sol of $FeMnO_3$ particles was diluted to achieve 0.1 mg ml^{-1} solid content. The pH was varied between 3 and 12 by adding HCl and NaOH. All measurements were performed at a given kinetic state followed by a minute of relaxation. The average values of the hydrodynamic diameter were calculated as the number weighted size from fits of the correlation functions.

The nitrogen isotherm at 77 K was collected on a Sorptomatic 1990 Thermo Finnigan (Thermo Scientific, UK), while all textural parameters were determined using the ADP 5.13 software (Thermo Electron). The powder sample was degassed for 36 h at 110 °C in vacuum. The specific surface area was calculated using the Brunauer–Emmett–Teller (BET) method. Mercury porosimetry measurements were performed on a high pressure unit PASCAL 440 (Thermo) in a CD3-P type dilatometer in the pressure range 0.1–200 MPa. Prior to analysis, the powder sample was dried at 110 °C for 24 h in an oven and additionally evacuated for 2 h in a sample holder at the analytical position of a Macropore Unit 120 (Carlo Erba) used for mercury filing of the dilatometer and bulk density determination. Two intrusion–extrusion runs were conducted, one after the other. A SOLID Software System PC interface was used for automatic data acquisition and all textural parameter calculations.

Measurement of ion release

Metal ion release from particle suspensions was investigated using ICP-OES on an iCAP-6500 Duo device (Thermo Scientific, UK). Iron manganite powder was first dried for 24 h at 110 °C in vacuum. 0.0997 g of dry iron manganite powder was added to 100 ml of distilled water or LB medium and mixed every 15 minutes for 4 h. It was then left to rest for 20 h. Five ml of particle suspension was taken using an automatic pipette and filtered through a 0.2 μm nylon syringe filter twice to remove powder particles. This solution was analysed for metal ion release. The lines at 257.610 and 238.204 were selected for Mn and Fe measurement, respectively. Concentrations of both cations were determined by the calibration curve method. The certified Specpure 42885 Alfa Aeser multi-element standard was used for preparing the calibration curve.

Evaluation of reactive oxygen species (ROS) release

An XTT (2,3-bis(2-methoxy-4-nitro-5-sulfophenyl)-2*H*-tetrazolium-5-carboxanilide, Sigma) assay was used to verify the production of a superoxide radical ion ($O_2^{\bullet -}$) by $FeMnO_3$ particles. XTT absorbs light at 470 nm only when reduced by $O_2^{\bullet -}$ and does not in its oxidized form. The ROS formation was observed in distilled water, LB (Luria–Bertani) and BHI (Brain Heart Infusion) media with and without UV irradiation. Different concentrations of particles were mixed with 0.2 mM XTT, and incubated in dark for overnight. 200 μl of each mixture were then deposited into 96 well-plate and the absorbance was monitored using an UV-vis spectrophotometer (Tecan infinite M200PRO). When the effect of UV was examined, the solutions were exposed to UV for 1 hour prior to the addition of 0.2 mM XTT.

The production of peroxyl and hydroxyl radicals was estimated by the fluorescence of 2′,7′-dichlorodihydrofluorescein diacetate (DCFH-DA) that may detect ROS inside and outside of the cells.[52] The excitation/emission peaks were at 503/523 nm, respectively. The fluorescence was monitored over time using an UV-vis spectrophotometer (Tecan infinite M200PRO) in 200 μM DCFH-DA solution inoculated with 10^6 CFU ml^{-1} bacterial cells. ROS variation was obtained comparing the fluorescence intensities of different walls containing 1 mg ml^{-1} $FeMnO_3$ with that without particles. All experiments were performed in 6 replicates.

Effect of iron manganite on bacterial growth

The *Bacillus subtilis* NDmed strain used in this study was kindly provided by Dr Roman Briandet (INRA, France). NDmed was isolated from an endoscope washer disinfector in a hospital in England.[53] NDmed was cultivated in Luria–Bertani (LB) or (Brain Heart Infusion) BHI broth at 37 °C, under shaking (200 rpm). Overnight cultures were diluted at least 100 fold in fresh medium in the presence of different concentrations of nanoparticles (0, 0.001, 0.005, 0.1 or 1 mg ml^{-1}). Growth curves were done in 96-well plates in a Tecan plate reader (Tecan infinite M200PRO) with continuous agitation at 37 °C absorption was measured at 600 nm.

Antioxidant activity

The antioxidant activity of $FeMnO_3$ was evaluated using 1,1-diphenyl-2-picrylhydrazyl radicals (DPPH) free radical assay. $FeMnO_3$ particles in serial dilutions (0.002 mg ml^{-1} to 2 mg ml^{-1}) were admixed to 1 ml of methanolic solution containing 0.2 mM DPPH. The mixtures were vortexed and left to stand for 30 min in the dark. The absorbance was measured at 517 nm against the blank. The percent inhibition of DPPH free radical by $FeMnO_3$ particles was calculated using the following expression: % inhibition $= [(A_{blank} - A_{sample})/A_{blank}] \times 100$, where A_{blank} was the absorbance of the control (containing all reagents except the particles) and A_{sample} is the absorbance of the test compound. The minimum concentration of particles that inhibits 50% DPPH radical IC_{50} value (mg ml^{-1}) was also reported.

Conclusions

To summarize, $FeMnO_3$ nanocrystalline particles with a net-like structure and plate-like shape were synthesized by the sol–gel combustion process, structurally, morphologically and texturally characterized. Antibacterial activity of $FeMnO_3$ particles was noted, antibacterial activity of $FeMnO_3$ particles was noted, together with H_2O_2 release and Fe- and Mn-ions release in LB bacterial medium. The mode of action, antioxidant activity and antibacterial efficacy of $FeMnO_3$ particles need to be further studied. Nevertheless, our study strongly suggests that the mode of antibacterial action by which metal oxide particles inhibit bacteria proliferation depend on the surrounding medium. $FeMnO_3$ was not toxic to *B. subtilis* in BHI medium, but was highly toxic towards *B. subtilis* in LB medium. Understanding molecular mechanisms of medium action on metal ion release and ROS generation of metal oxide particles will help in developing new materials and improving both selectivity and efficiency of engineered particles with antimicrobial activity.

Conflicts of interest

There are no conflicts to declare.

Acknowledgements

The authors would like to express their gratitude to Jelena D. Vujancevic (ITS SASA) for FESEM measurements, to Milica Zivkovic (IMGGE) for medium supplying and to Roman Briandet (INRA) for the NDmed strain. This work was partly financed by the Ministry for Education, Science and Technological Development of the Republic of Serbia.

Notes and references

1 S. Laurent, S. Boutry and R. N. Muller, Metal oxide particles and their prospects for applications, in *Iron oxide nanoparticles for biomedical applications*, Elsevier, 2018, DOI: 10.1016/B978-0-08-101925-2.00001-2.
2 S. Stankic, S. Suman, F. Haque and J. Vidic, *J. Nanobiotechnol.*, 2016, **14**, 73.
3 W. Jiang, H. Mashayekhi and B. Xing, *Environ. Pollut.*, 2009, **157**, 1619–1625.
4 Y.-W. Baek and Y.-J. An, *Sci. Total Environ.*, 2011, **409**, 1603–1608.
5 S. Auger, C. Henry, C. Péchaux, N. Lejal, V. Zanet, M. V. Nikolic, M. Manzano and J. Vidic, *Ecotoxicol. Environ. Saf.*, 2019, **182**, 109421.
6 J. Borcherding, J. Baltrusatis, H. Chen, L. Stebounova, C.-M. Wu, G. Rubasinghege, I. A. Mudunkotuwa, J. C. Caraballo, J. Zabner, V. H. Grassian and A. P. Comellas, *Environ. Sci.: Nano*, 2014, **1**, 123–132.
7 L. Wang, L. C. Hu and L. Shao, *Int. J. Nanomed.*, 2017, **12**, 1227–1249.
8 S. Auger, C. Henry, C. Longin, S. Shuman, N. Lejal, N. Bertho, T. Larcher, S. Stankic and J. Vidic, *Sci. Rep.*, 2018, **8**, 12276.
9 Y. H. Leung, A. M. C. Ng, X. Xu, Z. Shen, L. A. Gethings, M. T. Wong, C. M. Chan, M. Y. Gao, Y. H. Ng, A. B. Djurisic, P. K. H. Lee, W. K. Chan, L. H. Yu, D. L. Philips, A. P. Y. Ma and F. C. C. Leung, *Small*, 2014, **10**, 1171–1183.
10 A. H. Ashour, A. I. El-Batal, M. I. A. A. Maksoud, G. S. El-Sayyad, S. Labib, E. Abdeltwab and M. M. El-Okr, *Particuology*, 2018, **40**, 141–151.
11 P. Gong, H. Li, X. He, K. Wang, J. Hu, W. Tan, S. Zhang and X. Yang, *Nanotechnology*, 2007, **18**, 285604.
12 Y. Li, W. Zhang, J. Niu and Y. Chen, *ACS Nano*, 2012, **6**, 5164–5173.
13 V. Zanet, J. Vidic, S. Auger, P. Vizzini, G. Lippe and L. Iacumin, *J. Appl. Microbiol.*, 2019, **127**, 1391–1402.
14 N. Sharma, S. Jandaik, S. Kumar, M. Chitkara and I. S. Sandhu, *J. Exp. Nanosci.*, 2016, **11**, 54–71.
15 M. A. Islam, D. W. Morton, B. B. Johnson, B. Mainali and M. J. Angove, *J. Water Process Eng.*, 2018, **26**, 264–280.
16 A. Cetin, A. M. Onal and E. N. Esenturk, *J. Mater. Res.*, 2019, **34**(18), 1–9.
17 K. Cao, H. Liu, X. Xu, Y. Wang and L. Jiao, *Chem. Commun.*, 2016, **52**, 11414–11417.
18 C. Doroftei, P. D. Popa, E. Rezlescu and N. Rezlescu, *Composites, Part B*, 2014, **67**, 179–182.
19 M. Li, W. Xu, W. Wang, Y. Liu, B. Cui and X. Guo, *J. Power Sources*, 2014, **248**, 465–473.
20 B. Saravanakumar, S. P. Ramachandran, G. Ravi, V. Ganesh, R. K. Guduru and R. Yuvakkumar, *Mater. Res. Express*, 2018, **5**, 015504.
21 P. B. Mungse, G. Saravanan, M. Nishibori, J. Subrt and N. K. Labhsetwar, *Pure Appl. Chem.*, 2017, **89**, 511–521.
22 L. Leontie, C. Doroftei and A. Carlescu, *Appl. Phys. A*, 2018, **124**, 750.
23 M. V. Nikolic, M. D. Lukovic and N. J. Labus, *J. Mater. Sci.: Mater. Electron.*, 2019, **30**, 12399–12405.
24 M. H. Habibi and V. Mosavi, *J. Mater. Sci.: Mater. Electron.*, 2017, **28**, 10270–10276.
25 M. H. Habibi and V. Mosavi, *J. Mater. Sci.: Mater. Electron.*, 2017, **28**, 8473–8479.
26 S. Rayaprol and S. D. Kaushik, *Ceram. Int.*, 2015, **41**, 9567–9571.
27 I. Malaescu, A. Lungu, C. N. Marin, P. Vlazan, P. Sfirloaga and G. M. Turi, *Ceram. Int.*, 2016, **42**, 16744–16748.
28 S. Gowresan and A. Ruban Kumar, *Appl. Phys. A*, 2017, **123**, 689.
29 D. Gosh, U. Dutta, A. Haque, N. E. Morvidonova, O. I. Lebedev, K. Pal, A. Gayen, P. Mahata, A. K. Kundu and M. M. Seikh, *Mater. Sci. Eng., B*, 2017, **216**, 206–210.
30 R. H. Michna, B. Zhu, U. Mäder and J. Stülke, *Nucleic Acids Res.*, 2015, **44**, D654–D662.
31 H. P. Bais, R. Fall and J. M. Vivanco, *Plant Physiol.*, 2004, **134**, 307–319.
32 K. Momma and F. Izumi, *J. Appl. Crystallogr.*, 2011, **44**, 1271–1276.
33 S. Geller, *Acta Crystallogr., Sect. B: Struct. Crystallogr. Cryst. Chem.*, 1971, **27**, 821–828.

34 B. Kolk, A. Albers, I. R. Leith and M. G. Howden, *Appl. Catal.*, 1988, **37**, 57–74.
35 M. Thommes, K. Kaneko, A. V. Neimark, J. P. Olivier, F. Rodriguez-Reinoso, J. Rouquerol and K. S. W. Sing, *Pure Appl. Chem.*, 2015, **87**, 1051–1069.
36 J. Tauc, A. Menth and D. L. Wood, *Phys. Rev. Lett.*, 1970, **25**, 749–752.
37 R. López and R. Gómez, *J. Sol-Gel Sci. Technol.*, 2012, **61**, 1–7.
38 H. Bin, Z. Yao, S. Zhu, C. Zhu, H. Pan, Z. Chen, C. Wolverton and D. Zhang, *J. Alloys Compd.*, 2017, **695**, 1223–1230.
39 N. W. Roehm, G. H. Rodgers, S. M. Hatfield and A. L. Glasebrook, *J. Immunol. Methods*, 1991, **142**, 257–265.
40 R. G. Saratale, G. Kumar, G. Benelli, G. S. Ghodake, Y. Y. Jiang, D. S. Kim and G. D. Saratale, *Environ. Sci. Pollut. Res.*, 2018, **25**, 10250–20263.
41 K. Balan, W. Qing, Y. Wang, X. Liu, T. Palvannan, Y. Wang, F. Ma and Y. Zhang, *RSC Adv.*, 2016, **6**, 40162.
42 J. D. Aguirre and V. C. Culotta, *J. Biol. Chem.*, 2012, **287**, 13541–13548.
43 J. P. Lisher and D. P. Giedroc, *Front. Cell. Infect. Microbiol.*, 2013, **3**, 91.
44 A. Anjem, S. Varghese and J. Imlay, *Mol. Microbiol.*, 2009, **72**, 844.
45 P. Randazzo, J. Anba-Mondoloni, A. Aubert-Frambourg, A. Guillot, C. Peshoux, J. Vidic and S. Auger, *J. Bacteriol.*, 2020, **202**(5), e00547.
46 J. Vidic, F. Haque, J. M. Guigner, A. Vidy, C. Chevalier and S. Stankic, *Langmuir*, 2014, **30**, 11366.
47 T. H. Flo, K. D. Smith, S. Sato, D. J. Rodriguez, M. A. Holmes, R. K. Strong, S. Akira and A. Aderem, *Nature*, 2004, **432**, 917.
48 T. E. Kehl-Fie and E. P. Skaar, *Curr. Opin. Chem. Biol.*, 2010, **14**, 218.
49 U. Kadiyala, E. S. Turali-Emre, J. H. Bahng, N. A. Kotov and J. S. VanEpps, *Nanoscale*, 2018, **10**, 4927.
50 B. H. Toby and R. B. Von Dreele, *J. Appl. Crystallogr.*, 2013, **46**, 544–549.
51 H. Dachs, *Z. Kristallogr.–Cryst. Mater.*, 1956, **107**, 370–395.
52 H. Possel, H. Noack, H. Augustin, G. Keilhoff and G. Wolf, *FEBS Lett.*, 1997, **416**, 175–178.
53 D. J. H. Martin, S. P. Denyer, G. McDonnell and J.-Y. Maillard, *J. Hosp. Infect.*, 2008, **69**, 377–383.

